Title: Motor-Like Properties of Non-Motor Enzymes

Authors: David R. Slochower[a] and Michael K. Gilson[a]

Affiliations: [a] Skaggs School of Pharmacy and Pharmaceutical Sciences, University of California San Diego, La Jolla, California 92093-0736, United States.

Corresponding author: Michael K. Gilson, E-mail: mgilson@ucsd.edu, Telephone: 858-822-0622, Skaggs School of Pharmacy and Pharmaceutical Sciences, University of California San Diego, La Jolla, California 92093-0736, United States.

Keywords: Molecular motors, protein dynamics, protein evolution

Abstract

Molecular motors are thought to generate force and directional motion via nonequilibrium switching between energy surfaces. Because all enzymes can undergo such switching, we hypothesized that the ability to generate rotary motion and torque is not unique to highly adapted biological motor proteins, but is instead a common feature of enzymes. We used molecular dynamics simulations to compute energy surfaces for hundreds of torsions in three enzymes, adenosine kinase, protein kinase A, and HIV-1 protease, and used these energy surfaces within a kinetic model that accounts for intersurface switching and intrasurface probability flows. When substrate is out of equilibrium with product, we find computed torsion rotation rates up ~140 cycle s^{-1}, with stall torques up to ~2 kcal mol^{-1} $cycle^{-1}$, and power outputs up to ~50 kcal mol^{-1} s^{-1}. We argue that these enzymes are instances of a general phenomenon of directional probability flows on asymmetric energy surfaces for systems out of equilibrium. Thus cyclic probability fluxes, corresponding to rotations of torsions and higher-order collective variables, are expected in any chiral molecule driven between states in a non-equilibrium manner. The same considerations apply to synthetic chiral molecules switched in a nonequilibrium manner between energy surfaces by light, redox chemistry, or catalysis.

Text

Introduction

A biological molecular motor is an enzyme that uses the free energy of an out-of-equilibrium chemical reaction to drive mechanical motion. This motion must have a specific direction to fulfill the motor's functional role; for example, a helical flagellum must rotate in the appropriate sense to propel the organism. The ability to generate a directional cycle of conformational changes appears to be a highly specialized protein property. However, it has been argued that a key mechanistic aspect of biomolecular motors is that they are switched in a nonequilibrium manner between distinct energy surfaces (1-8), and non-motor enzymes also switch between at least two conformational free energy surfaces as they bind and release substrate. It is thus of interest to ask whether enzymes not normally thought of as motor proteins have motor-like properties when operating away from chemical equilibrium.

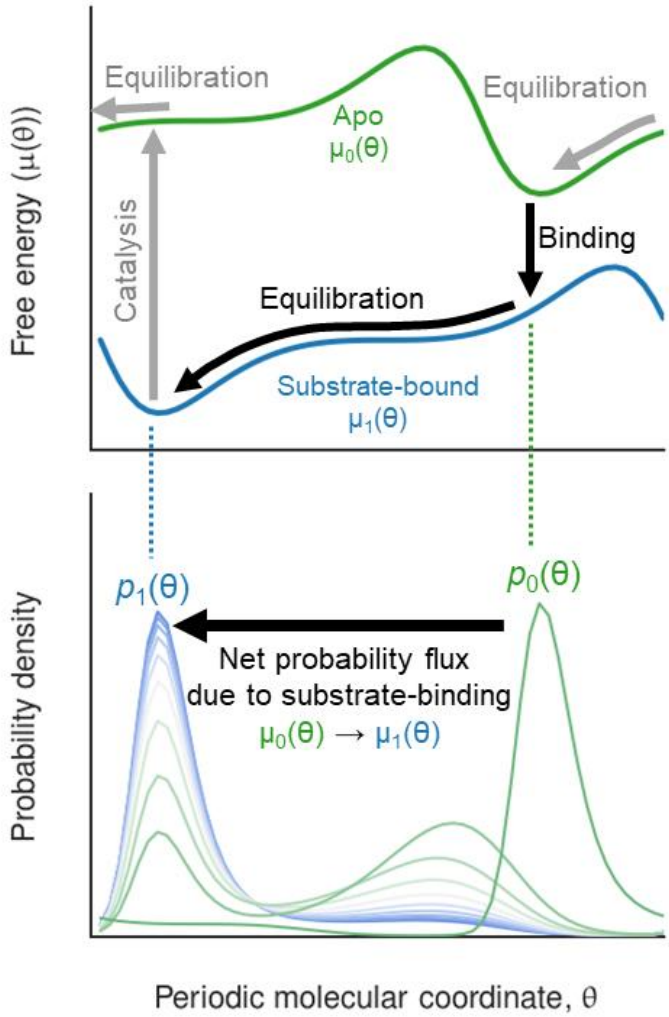

Fig. 1. Illustrative apo and substrate-bound free energy surfaces of an enzyme (solid green and blue lines, respectively) and the flow of probability along coordinate θ, after the effective potential changes due to substrate binding (green to blue probability distribution curves).

Consider a periodic molecular coordinate, θ, such as a bond torsion or a higher-order collective variable, in an enzyme undergoing a catalytic cycle of substrate-binding, catalysis, and product release. When binding of substrate switches the effective energy surface from that of the apo state, $\mu_0(\theta)$, to that of the bound state, $\mu_1(\theta)$, probability flows along θ towards a new equilibrium distribution corresponding to $\mu_1(\theta)$ (Figure 1). Such a flow of probability can be modeled with the Fokker-Planck equation, for example

(4). Because enzymes are chiral, neither energy landscape, $\mu_0(\theta)$ and $\mu_1(\theta)$, can possess mirror symmetry; i.e., neither can be an exactly even function around any value of θ. Thus, there will be more probability flow in one direction than the other, due to the asymmetry of the starting probability distribution and of the patterns of barriers and troughs along the bound free energy surface. After the substrate is catalytically removed, this process repeats itself, with a probability distribution that has approached equilibrium on the substrate-bound surface diffusing asymmetrically under the potential of the apo free energy surface, $\mu_0(\theta)$. Unless there is an infinitely high energy barrier at the same location on both surfaces, there is no basis to expect that the net flows will cancel identically for a chiral molecule, and the resulting asymmetric net flow of probability during this two-step process constitutes directional motion. Note that any such motion will be superimposed on a background of rapid, non-directional stochastic fluctuations in θ.

As this reasoning is general in nature, we hypothesized that all periodic coordinates of any enzyme catalyzing an out-of-equilibrium reaction must undergo some degree of directional rotations. In order to uncover these rotations and begin to assess their magnitudes, we used molecular simulations and kinetic analysis to analyze the rotational dynamics of bond torsions induced by nonequilibrium, stochastic, state-switching in three, diverse, non-motor enzymes: adenosine kinase (ADK), protein kinase A (PKA), and HIV-1 protease (HIVP).

Materials and Methods

The one-dimensional free energy surfaces of protein main- and side-chain torsions, discretized into bins, were obtained from equilibrium molecular dynamics (MD) simulations of the enzymes in their apo and substrate-bound states (Supplementary Methods). These data, coupled with literature values for the enzyme kinetic parameters (Table S1), enabled us to define first order rate constants for transitions along and between the free energy surfaces (Fig. S1). The resulting set of rate equations was solved for the non-equilibrium steady state probability distribution, for a given concentration of substrate, and this, in turn, was used to compute the probability flux on each surface. The net flux, J, in units of torsional rotational cycles per second, is an indication of directional rotation; e.g., a positive value implies clockwise rotation of the torsion.

The three non-motor enzymes studied have distinctive characteristics: adenylate kinase (ADK), with 214 residues and a relatively high k_{cat} ~300 s^{-1} (9, 10), undergoes extensive conformational change on binding substrate, with two domains reorienting to form a compact conformation (11, 12); protein kinase A (PKA), with 350 residues and k_{cat} ~140 s^{-1} (13), acts as a “dynamic switch”, with long-range allosteric interactions and domain rearrangement upon ligand binding (14); and HIV-1 protease (HIVP), with 200 residues and lower k_{cat} ~10 s^{-1} (15-17), contains two flexible flaps that lose mobility in the substrate-bound state (18, 19) (Fig. S2).

Results

For all three enzymes, we find that multiple torsion angles undergo directional rotations, as indicated by nonzero probability flux, when excess substrate is present. Thus, at high

substrate concentration, about 40 torsions in ADK and PKA rotate faster than 10 cycle s^{-1}, and about 140 rotate faster than 1 cycle s^{-1} (Fig. 2a). Directional rotation is also observed for HIVP, though the rates are lower (Fig. 2b, red). The lower rates largely reflects the lower k_{cat} value of HIVP, relative to PKA and ADK. Thus, artificially assigning $k_{cat} = 200\ s^{-1}$ to HIVP leads to substantial increases in the number of torsions with fluxes of at least 10 s^{-1} and at least 1 s^{-1} (Fig. 2b, orange and Fig. S3). The tendency toward lower fluxes in HIVP may also reflect the smaller scale of its conformational changes (Fig. S2): a small conformational change may lead to more similar energy surfaces in the two states, and hence less opportunity to generate rotational flux by the mechanisms discussed below.

Although the maximum rotation rates are different for ADK, PKA and HIVP (180, 70 and 5.6 s^{-1}, respectively), the maximum numbers of rotations per catalytic step are similar, at 0.5 – 0.6 cycles per catalytic turnover (Fig. 3). (Assuming $k_{cat} = 200\ s^{-1}$ for HIVP yields a maximum rate of 112 cycles s^{-1}, which corresponds to 0.6 cycles per catalytic turnover.) This ratio is akin to a 2:1 gearing of catalysis to torsional rotation. Figs. S3 and S4 provide further details regarding the relationships between catalytic rate and torsional flux for additional torsions. The angles with highest directional flux are localized near the substrate binding pocket or mobile regions (Fig. S2).

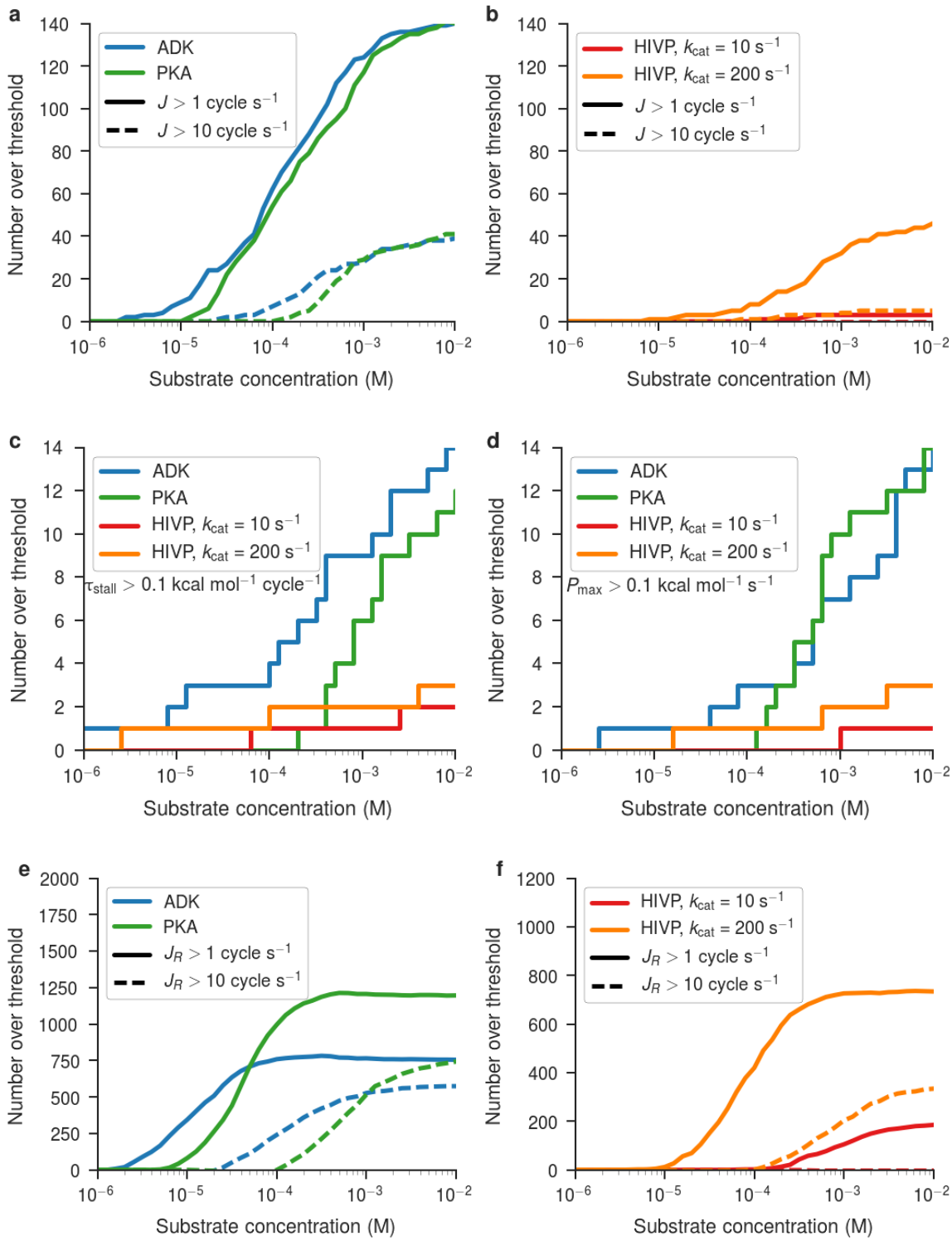

Fig. 2. The number of torsions above various thresholds of directional flux magnitude, reciprocating flux magnitude, stall torque, and maximum power, as a function of substrate concentration. (a-b) The number of torsions with directional flux above 1 (solid) or 10 (dotted) cycle s^{-1} in ADK, PKA, and HIVP. (c-d) The number of angles with (c) maximum stall force above 0.1 kcal/(mol·cycle) and (d) power above 0.1 kcal/(mol·s^{-}

[1]). (e-f) The number of torsions with reciprocating flux above 1 (solid) or 10 (dotted) cycle s^{-1} and, at the same time, directional flux less than 1 cycle s^{-1}.

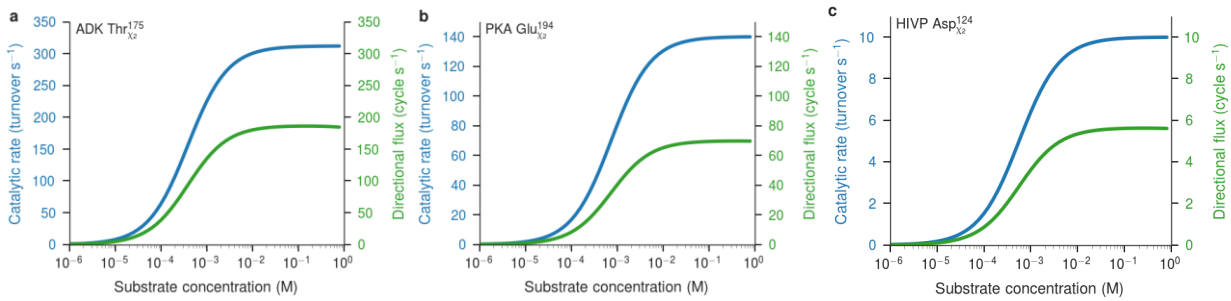

Fig. 3. Dependence of catalytic rates and of the magnitude of directional flux on substrate concentration, for torsion angles in each enzyme. (a) The χ_2 angle of Thr175 in ADK reaches a high level of directional flux. (b) The χ_2 angle of Glu194 in PKA reaches a moderate level of directional flux. (c) Although the total amount of flux in the χ_2 angle of Asp124 in HIVP is low, the ratio of directional flux to the enzyme velocity is similar to that in ADK and PKA.

We furthermore evaluated power output and performance under load by tilting the energy surfaces to generate a torque, τ, opposite to the directional flux, which modifies the intrasurface bin-to-bin rate constants (Supplementary Methods). The power output is the product of load torque and flux: $P = \tau J$. Both the maximum power and the stall torque, τ_{stall}, defined as the torque that brings the directional flux to zero, were found by scanning across values of applied torque. The results indicate that torsions in these enzymes can do work against small mechanical loads and thus generate power (Fig. 2c,d). In particular, at high substrate concentrations, torsions in ADK and PKA are predicted to generate stall torques up to 2.4 and 1.6 kcal mol^{-1} $cycle^{-1}$, respectively, and maximum power outputs per torsion of 70 and 28 kcal mol^{-1} s^{-1}.

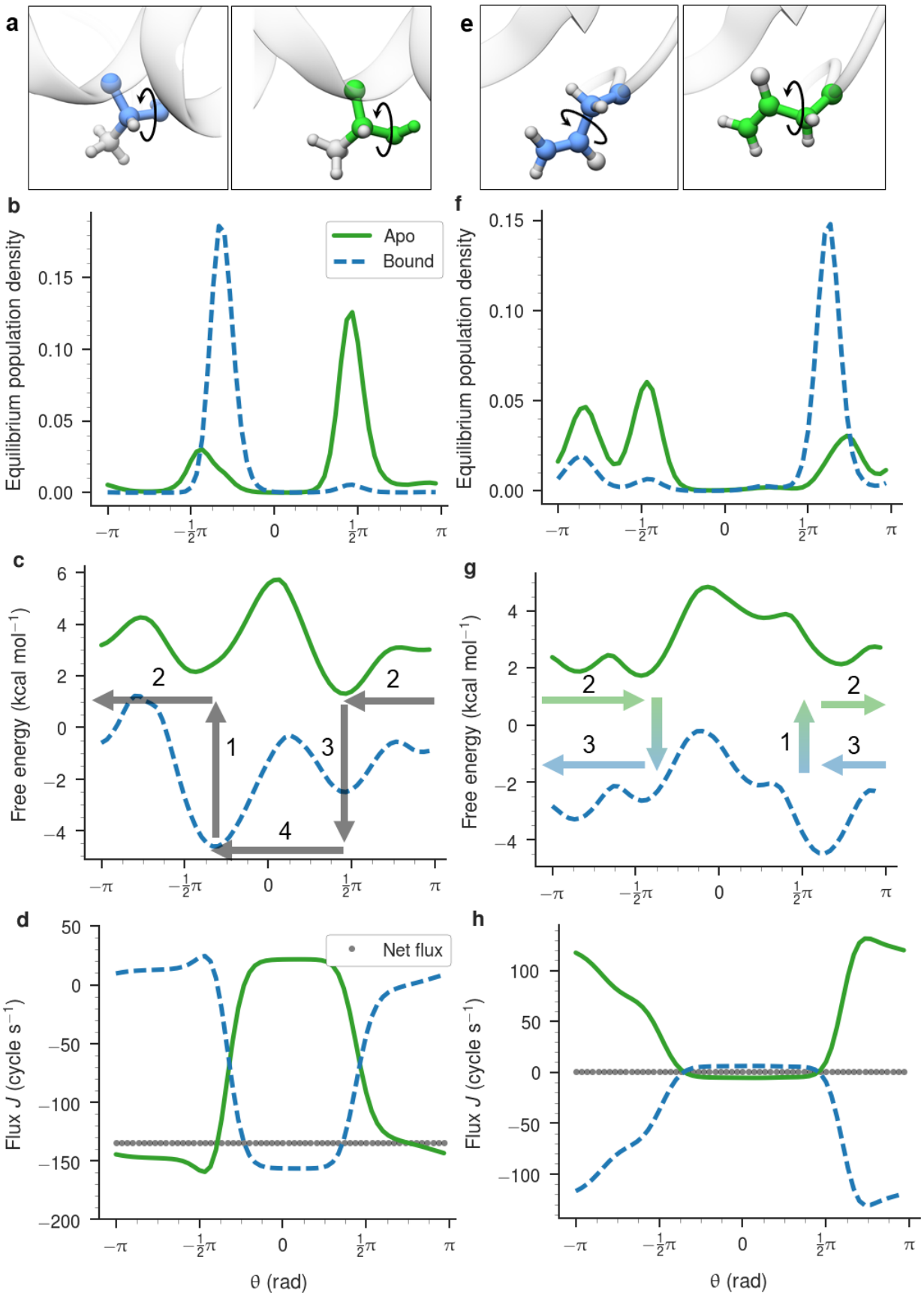
a
e
b
f
Equilibrium population density
Apo
Bound
c
g
Free energy (kcal mol^{-1})
1
2
3
4
d
h
Flux J (cycle s^{-1})
Net flux
θ (rad)

Fig. 4. Protein torsion angles show directional and reciprocating motion. (a) ADK Thr175 in its crystallographic conformations for the apo (green) and bound (blue) forms (see Supplementary Methods for PDB accessions) with the χ_2 angle denoted. The coloring is the same for panels a through d. (b) Equilibrium population densities of this angle from MD simulations (Supplementary Methods). (c) Free energy surfaces of this angle (Supplementary Methods) derived from the population densities in panel b. Arrows indicate the direction of probability flux along, and between, the two surfaces. (d) The probability flux drawn separately for each surface and as a sum (grey points), indicating large directional and reciprocating fluxes. (e-h) Same as a-d for ADK Asn138. In all cases the substrate concentration is 10^{-3} M.

The mechanism by which high rates of directional flux are generated is illustrated by the χ_2 torsion of ADK Thr175 (Fig. 4a). This angle has a two-peaked probability distribution in both the bound and apo states, but the peak near $+\frac{\pi}{2}$ is favored in the apo state, while that near $-\frac{\pi}{2}$ is favored in the bound state (Fig. 4b,c). In the presence of substrate, the bound-state energy minimum near $-\frac{\pi}{2}$ is highly occupied (Fig. 4b,c). Catalytic breakdown of substrate pumps the system to the secondary energy minimum of the apo state at $-\frac{\pi}{2}$ (Fig. 4c, arrow 1). Probability then flows primarily to the left on the apo surface, because this is the lowest-barrier path to the apo state's global energy minimum near $+\frac{\pi}{2}$ (arrow 2; this flux goes through the periodic boundary at $\theta = -\pi \equiv +\pi$). Probability pooled in the global energy minimum of the apo state near $+\frac{\pi}{2}$, then flows primarily to the bound state, by binding substrate and landing in the secondary energy minimum of the bound state (arrow 3). It then flows back to the global minimum of the bound state via the lowest-barrier path, which is again leftward (arrow 4). The net effect is a leftward flux of up to -140 cycles s^{-1}. Fig. 4d shows the steady state flux on each surface: leftward flux predominates overall, but occurs on the apo surface between

$-\frac{\pi}{2}$ and $+\frac{\pi}{2}$, and on the bound surface elsewhere, with crossovers between surfaces at the energy minima.

This process parallels fluctuating potential mechanisms previously invoked to explain highly evolved molecular motors (3, 4, 7, 8, 20-23). Intuitively, high flux can be generated when each energy surface (apo and bound) has a main energy barrier and a main energy well, and the two surfaces are offset, so that probability flow in a given direction on each surface bypasses the barrier on the other surface, as schematized in Fig. S5 a-b. Also, as noted above, generation of net flux requires asymmetric energy surfaces; i.e., energy surfaces that are not even functions around any value of θ. Accordingly, symmetrizing the energy surfaces of a high-flux torsion abolishes directional flux, as shown in Fig. S6.

There are also many torsions whose net directional flux is small (< 1 cycle s^{-1}), and whose dynamics are instead dominated by reciprocating motion, in which probability flows in one direction in the bound state and in the other direction in the apo state, within some angular range. These reciprocating probability fluxes correspond to driven, oar-like motion of the atoms controlled by the torsion. The enzymes ADK and PKA, respectively, are predicted to have ~1250 and ~750 torsions with reciprocating motions at rates of at least 1 cycle s^{-1} (Fig. 2e,f), and minimal directional flux. The maximal reciprocating fluxes are greater than the maximal directional fluxes, and, for ADK and PKA, approach the catalytic rates (Fig. S4). The mechanism of reciprocating motion is illustrated by χ_2 of Asn 138 in ADK (Fig. 4e), which has a net flux that is nonzero but well below 1 cycle s^{-1}, yet has reciprocating fluxes of up to 130 cycles s^{-1} (Fig. 4e-h). Reciprocating flux occurs when the main energy wells on the two surfaces

are in different locations, but little probability flow on each surface bypasses the main barrier on the other surface, as schematized in Fig. S5 c-d. Thus, if the main barriers in the two states are coincident, movement will be dominated by reciprocating motion.

Discussion

We have provided reasoning and evidence that directional rotation that can work against a load is not limited to highly adapted biological motor proteins. Instead, any enzyme operating out of equilibrium should generate directional conformational fluxes. The magnitudes of these motions will depend on a number of factors, including the levels and locations of the barriers and energy wells on the two surfaces, and the chemical driving forces and kinetic constants. We also observe high reciprocating flux in torsions with energy surfaces that are not well tuned to generate net directional motion. The present modeling approach uses atomistic modeling to obtain the effective potentials, and then embeds these in a kinetic model. This efficient technique is more broadly applicable, and could be used to study not only proteins but also synthetic molecular motors. This approach can also be extended to account for greater complexity, such as a position-dependent diffusion constant and additional energy surfaces. Although we have focused on torsional motions, the same reasoning applies to motions through higher-order conformational subspaces, including larger-scale protein domain motions, because they, too, will have asymmetric potentials, due to the chirality of these molecules. Such motions might help explain the observation that the translational diffusion coefficients of some enzymes rise with substrate concentration and hence with enzyme velocity (24, 25). The present results also indicate that even

enzymes from earliest evolutionary time would have had the ability to generate directional motion, and thus would have had a good starting point from which to embark on an evolutionary path to today's highly adapted motor proteins.

Acknowledgments

We thank Dr. N.-L. Huang for assistance preparing simulations on ADK and HIVP; Mr. M. Feng and Drs. A. Gilson, K. Lindenberg, C. Van den Broeck, and J.A. McCammon for theoretical discussions; and Dr. C. McClendon for providing the PKA simulations. This work was funded in part by grant GM061300 from the National Institutes of Health (NIH). Its contents are solely the responsibility of the authors and do not necessarily represent the official views of the NIH.

M.K.G. has an equity interest in and is a cofounder and scientific advisor of VeraChem LLC.

The datasets generated and analyzed during the current study are available in the GitHub repository https://github.com/GilsonLabUCSD/nonequilibrium.

M.K.G. conceived and designed the project. D.R.S. implemented the model and performed the simulations. M.K.G. and D.R.S. analyzed the data and wrote the manuscript.

Supporting Material

Fluctuating potential kinetic model

Definition of the model

The enzyme is considered to have two chief macrostates, apo (P_0) or substrate-bound (P_1), and is assumed to follow Michaelis-Menten kinetics:

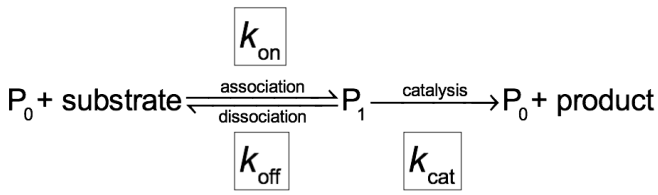

Thus, the substrate-bound protein can reach the apo state either through dissociation of the substrate or through catalytic conversion of the substrate into the product, followed by dissociation of the product. The substrate concentration is left as an adjustable parameter, while, the concentration of product is considered low enough that the reverse reaction makes no significant contribution to the kinetics.

The equilibrium probability distribution functions of the torsion angles of interest, in protein states P_0 and P_1, were obtained as follows. Torsional histograms, each with N bins, were computed from the equilibrium MD simulations described below, and converted to probabilities by normalization. The resulting probability distributions were smoothed with a Gaussian kernel (standard deviation of 1 bin), and any bins with zero probability after smoothing were assigned the lowest probability observed in any bin for that angle (typically about 10^{-6}). Following normalization, the resulting probabilities are $p_{0,i}$ and $p_{1,i}$ for bin i in the apo and substrate-bound states, respectively, where $\sum_{i=1}^{N} p_{0,i} = \sum_{i=1}^{N} p_{1,i} = 1$. The present results are based on $N = 60$, which captures the

shapes of the energy surfaces without imposing an excessive computational burden. Using fewer bins would effectively smooth the surfaces, reducing the differences between apo and bound and thus decreasing the computed fluxes and torques.

The kinetic model allows transitions between neighboring bins in the same state, with forward and reverse rate constants $k_{x,i\to i+1}$ and $k_{x,i+1\to i}$ respectively, where $x = 0$ for the apo state and $x = 1$ for the bound state; and transitions between states in the same bin, with rate constants $k_{0\to 1,i}$ and $k_{1\to 0,i}$ for binding and dissociation, respectively. These intersurface rate constants are set to

$$k_{0\to 1,i} = k_{\text{on}} C_S \tag{1}$$

where k_{on} is the macroscopic on-rate for binding of substrate to the enzyme and C_S is the substrate concentration; and

$$k_{1\to 0,i} = k_{\text{on}}\, e^{\Delta G_i/RT} \tag{2}$$

where ΔG_i, the binding free energy associated with bin i, is given by

$$\Delta G_i = \mu_{1,i} - \mu_{0,i} \tag{3}$$

where $\mu_{x,i}$ is the free energy associated with bin i on surface x:

$$\mu_{0,i} = -RT \ln p_{0,i} \tag{4}$$

$$\mu_{1,i} = -RT \ln p_{1,i} - RT \ln K_{\text{d}}$$

We now show that this set of rate constants leads to the correct dissociation constant, K_d, for the full system. In particular, because $K_{\text{d}} = C_1/C_0 C_S$, where C_1 and C_0 are the concentrations of bound and free protein, respectively, we want

$p_1/p_0 = C_1/C_0 = C_S/K_\mathrm{d}$, where p_0 and p_1 are the probabilities of finding the enzyme in the apo and bound states, respectively, so that $p_0 + p_1 = 1$. Using the fact that the equilibrium constant is the ratio of rate constants, and that the contribution of each bin's rate constant to the corresponding macroscopic rate constant is weighted by the probability of the bin, we have

$$\frac{p_1}{p_0} = \frac{\sum_{i=1}^{N} p_{0,i} k_{0\to 1,i}}{\sum_{i=1}^{N} p_{1,i} k_{1\to 0,i}} \tag{5}$$

Using the prior equations, we obtain

$$\frac{p_1}{p_0} = \frac{\sum_i^N p_{0,i}(k_\mathrm{on} C_S)}{\sum_i^N p_{1,i}(k_\mathrm{on}\, e^{\Delta G_i/RT})} = \frac{C_S}{\sum_i^N p_{1,i}\left(\frac{1}{p_{1,i}} p_{0,i} K_\mathrm{d}\right)} = \frac{C_S}{K_\mathrm{d}} \tag{6}$$

as required. This confirms that the intersurface rate constants in Eqs (1) – (2) correctly replicate the equilibrium between apo and bound enzyme in the absence of catalysis.

Transitions between neighboring bins on each energy surface are also modeled by first order rate processes, with the rate constants chosen to replicate free rotational diffusion in the limit of a flat energy surface, and to generate the MD-derived probability distribution on each surface in the absence of catalysis (see below):

$$k_{0,i\to i+1} = D\exp\left\{-\frac{\left(\mu_{0,i+1}-\mu_{0,i}\right)}{2RT}\right\} \tag{7}$$

$$k_{0,i+1\to i} = D\exp\left\{-\frac{\left(\mu_{0,i}-\mu_{0,i+1}\right)}{2RT}\right\}$$

$$k_{1,i\to i+1} = D\exp\left\{-\frac{\left(\mu_{1,i+1}-\mu_{1,i}\right)}{2RT}\right\}$$

$$k_{0,i+1\to i} = D\exp\left\{-\frac{\left(\mu_{1,i}-\mu_{1,i+1}\right)}{2RT}\right\}$$

The forward and reverse rate constants are equal to D if the energy difference between the two bins is zero, and any energy difference increases and decreases the forward and reverse rate constants, respectively, by the same factor, as expected on physical grounds. The value of D is discussed in Assignment of Numerical Parameters, below.

Solving the first order kinetic system described above would yield an equilibrium Boltzmann probability distribution across the bins and states,

$$p_{x,i}^{\mathrm{eq}} \propto \exp\left(-\frac{\mu_{x,i}}{RT}\right) \tag{8}$$

with the following normalization:

$$1 = \sum_{i}^{N}\left(p_{0,i}^{\mathrm{eq}} + p_{1,i}^{\mathrm{eq}}\right) \tag{9}$$

So far, we have included only one mechanism for transitioning from the bound state to the apo state: dissociative release of substrate. However, there is a second mechanism, which is the one that can put the system out of equilibrium, namely

catalytic degradation of the substrate followed by product release. Referring to Eq (2), we account for this by adding another set of first-order rate processes going from the bound state bins to the apo state bins, with rate constants of k_{cat}:

$$k_{1\to 0,i} = k_{\text{on}}\, e^{\Delta G_i/RT} + k_{\text{cat}} \tag{10}$$

As noted above, for simplicity, we assume that the concentration of product is negligibly small. When C_S and k_{cat} are nonzero, the system is no longer at equilibrium, but instead goes to a non-equilibrium, steady-state probability distribution, $p_{x,i}^{\text{ss}}$. This distribution is obtained by the numerical method described in the following subsection.

<u>Steady-state solution of the kinetic model</u>

The system of rate equations is discretized in time by multiplying each rate constant by a small time-interval Δt, yielding the fractional change in probability within each bin over this time. From these values, we construct a $2N \times 2N$ Markov transition matrix with off-diagonal elements that contain these fractional probability changes. The diagonal entries are then determined from the requirement that the sum of each row in the matrix equals 1. We used numerical methods (26, 27) to diagonalize the matrix, and the eigenvector whose eigenvalue value is unity corresponds to the steady state populations, $p_{x,i}^{\text{ss}}$ of all $2N$ bins in the system. The steady state probability flux between bins i and $i+1$ on surface x is then

$$J_{x,i} = p_{x,i}^{\text{ss}} k_{x,i\to i+1} - p_{x,i+1}^{\text{ss}} k_{x,i+1\to i}. \tag{9}$$

The net probability flux is the sum across both surfaces,

$$J_i \;= \left(p_{0,i}^{\text{ss}} k_{0,i\to i+1} - p_{0,i+1}^{\text{ss}} k_{0,i+1\to i}\right) + \left(p_{1,i}^{\text{ss}} k_{1,i\to i+1} - p_{1,i+1}^{\text{ss}} k_{1,i+1\to i}\right). \tag{10}$$

At steady state, J_i is uniform across bins, and we write $J \equiv J_i$ in the main text as "directional flux". We also report "reciprocating flux" for each torsion as the peak magnitude of directional flux across either surface, $J_R = \max(|J_{0,i}|, |J_{1,i}|)$.

<u>Applying a load (torque) to a torsion angle</u>

One test of these motors is their ability to do work against a mechanical load. We apply load by tilting the free energy surfaces with a constant slope, corresponding to a torque, τ, that opposes the direction of flux. This is done by supplementing the chemical potential differences in equation (4) with an energy difference ΔE, to generate rate expressions of the form

$$k_{0,i\to i+1} = D \exp\left\{-\frac{(\mu_{0,i+1} - \mu_{0,i} + \Delta E)}{2RT}\right\} \tag{11}$$

$$k_{0,i+1\to i} = D \exp\left\{-\frac{(\mu_{0,i} - \mu_{0,i+1} - \Delta \mathrm{E})}{2RT}\right\}$$

$$k_{1,i\to i+1} = D \exp\left\{-\frac{(\mu_{1,i+1} - \mu_{1,i} + \Delta E)}{2RT}\right\}$$

$$k_{0,i+1\to i} = D \exp\left\{-\frac{(\mu_{1,i} - \mu_{1,i+1} - \Delta E)}{2RT}\right\}$$

on both energy surfaces. That is, the energy difference between adjacent bins used to compute the transition rates (equation (9)) are modified by a factor $\pm\Delta E$, depending on direction, where $\Delta E > 0$ gives a negative torque that is used to oppose positive probability flux, and vice versa. So that the load is correctly imposed across the periodic boundary, we replace $\mu_{x,1} - \mu_{x,N}$ with $\mu_{x,1} - \mu_{x,N} + \Delta E$ and $\mu_{x,N} - \mu_{x,1}$ with $\mu_{x,N} - \mu_{x,1} - \Delta E$. The stall torque is the load that brings the next flux to zero; increasing the torque

beyond this limit will cause the motor to slip backwards. We identify the stall torque by solving the kinetic system iteratively for a systematic scan of applied torques. The power produced for a given torque is given by $P = \tau J_\tau$, where J_τ is the flux computed for a given applied torque τ. Empirically, the maximum power is found to occur at half the stall torque.

Assignment of numerical parameters

The present model requires numerical values of D, k_{on}, $K_{\mathrm{d}} = 1/K_{\mathrm{a}}$, and k_{cat}. An initial estimate of D was made by simulating a molecule of butane, with the force field torsion and nonbonded terms set to zero to create a flat energy surface, and determining the rotational diffusion constant for this barrierless torsion. The mean value over one hundred 1 ns Langevin dynamics simulations is 3×10^{15} degree^2 s^{-1}. However, this large value led to numerical instability during diagonalization of the transition matrix, so we tested how the computed fluxes vary with D, and found that they are insensitive to the value of D once it is above $\sim 10^9$ degree^2 s^{-1}. We used $D = 3 \times 10^{12}$ degree^2 s^{-1} for the present calculations, as this is well into the regime where the results are independent of D, but not so large as to cause numerical problems (Fig. S7). The enzyme kinetic parameters and their basis in the experimental literature are provided in Table S1.

Materials and Methods:

Torsion potentials of mean force from molecular dynamics simulations

Adenylate Kinase

PDB accession 4AKE (28) was used as a starting structure for apo ADK; crystallographically ordered water molecules were retained. Hydrogens were added with `pdb2pqr` (29) at pH 7.0, bringing the net charge of the protein to -4. The substrate-bound protein was similarly modeled using PDB accession 3HPQ (30), which includes the ligand AP5A, a transition state analog, bound to the active site. AP5A carries a charge of -5 on the five phosphate groups, and the protein again carries a charge of -4 in the bound state. Partial atomic charges for AP5A were determined using the AM1-BCC method (31) in the `antechamber` program, and the remaining force field parameters were assigned from GAFF (32, 33). The apo and substrate-bound simulation systems were neutralized with 4 and 9 sodium ions, respectively. Both protein structures were solvated in a truncated octahedron with 12 Å padding.

Each system was energy-minimized for 20,000 steps, thermalized to 300 K over 1 ns, and equilibrated for 100 ns. Production simulations were then carried out for 1.0 μs using PME electrostatics with a 9 Å cutoff, and hydrogen mass repartitioning (34) with a 4 fs time step, using `pmemd.cuda.MPI` module of Amber 16 (35). Histograms (60 bins) of the torsion types listed in Table S2 were computed over the entire production simulation, using the `cpptraj` module (36) of Amber 16.

HIV Protease

PDB accession 1HHP (37) was used to model the apo structure of HIV-1 protease; crystallographically ordered waters were retained. To be consistent with Uniprot P03367, we made the following computational mutations: K14R, S37N, R41K, L63P, and I64V. Hydrogens were added with `pdb2pqr` at pH 7.0, bringing the net charge of the protein to +4. The substrate-bound protein was modeled using PDB accession 1KJF (38) with 10 residues of the Gag protein co-crystallized (`RPGNFLQSRP`; residues 443-452; fragment p1-p6 or SP2-p6). The following mutations were made to make the apo and bound structures consistent: K7Q and N25D. The charge of the bound protein and peptide was +6. Both models were solvated in a truncated octahedron with 12 Å padding and 4 or 6 chloride ions, respectively, added to neutralize the charge. The simulation procedures were identical to those for ADK.

Protein Kinase A

Simulations were carried out as described in reference (14).

Numerical convergence

Convergence of the results was tested by using increasing amounts of simulation time to derive apo and bound state population histograms and then predicting the directional flux based on those histograms. For a sample angle shown in Fig. S8, after 500 ns, the calculated directional flux is very close to its value at 1000 ns, and the uncertainty in the flux value drops from about ±60 cycle s^{-1} to about ±1 cycle s^{-1} going from 500 ns to 1000 ns.

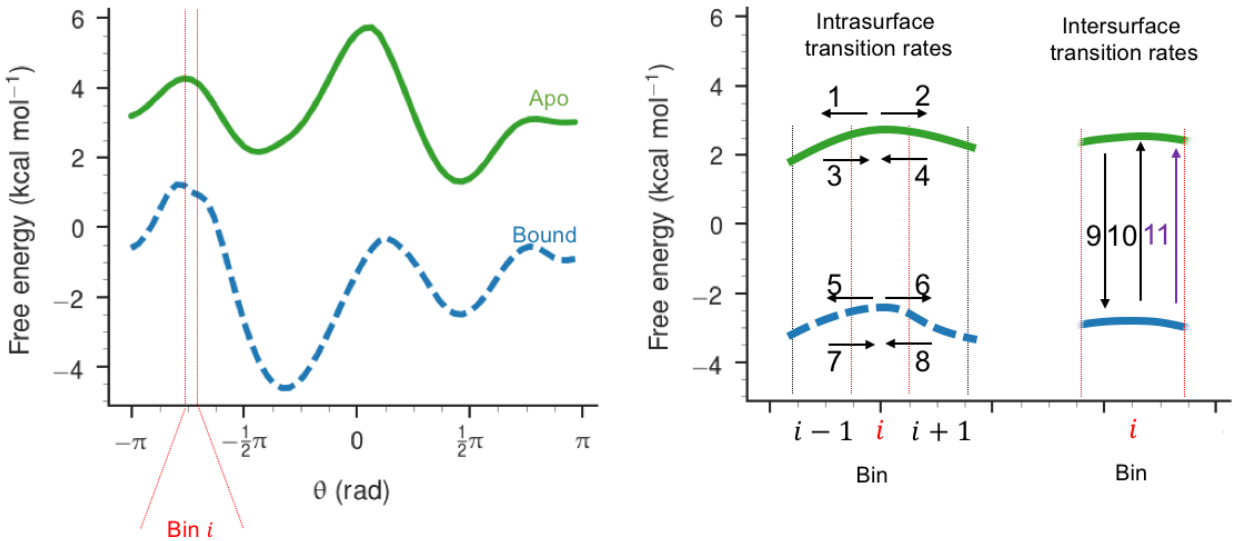

Fig. S1. Transitions in the kinetic model. Small segments of the apo (green) and bound (blue) surfaces are diagrammed, with boundaries between discretization bins denoted with vertical lines. For each bin i, there are transitions in both directions between i and $i-1$ (arrows 1 and 3) as well as between i and $i+1$ (arrows 2 and 4) on the apo surface; there are similar transitions on the bound surface (arrows 5 and 7 and arrows 6 and 8, respectively). In addition, for each bin i, there is a transition from the apo surface to the bound surface (arrow 9, substrate binding) a dissociative transition from the bound surface to the apo surface (arrow 10), and a catalytic transition from the bound surface to the apo surface (arrow 11).

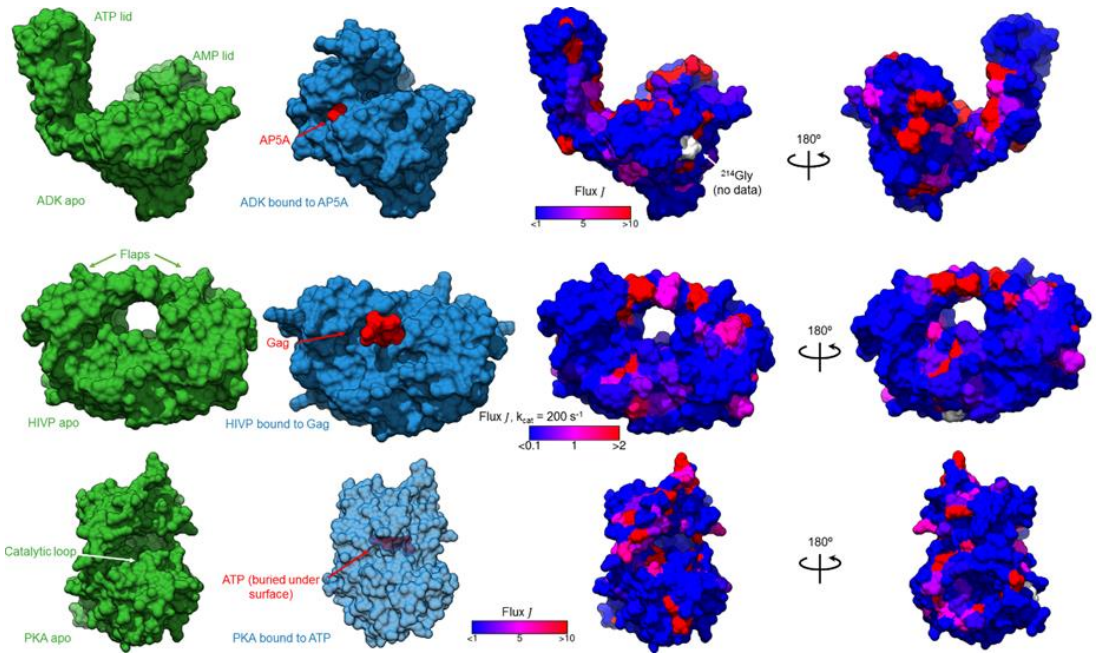

Fig. S2. The apo and substrate-bound structures of the enzymes studied. Top row: the apo (green; PDB accession 4AKE) and substrate-bound (blue; PDB accession 3HPQ) conformations of ADK, rendered as a surface, with substrate AP5A (red) as spheres. In the right two panels, the absolute magnitude of directional flux J is mapped onto the apo structure, using a color gradient with thresholds from < 1 cycle s^{-1} (blue) to > 10 cycle s^{-1} (red). Middle row: the apo (green; PDB accession 1HHP) and substrate-bound (blue; PDB accession 1KJF) conformations of HIVP, rendered as a surface, with substrate Gag peptide (red) as spheres. In the right two panels, the absolute magnitude of directional flux J is mapped onto the apo structure, using the same color gradient, with thresholds < 0.1 cycle s^{-1} (blue) to > 2 cycle s^{-1} (red), to account for the lower level of directional flux in HIVP, even at $k_{cat} = 200$ s^{-1}. Bottom row: the apo (green; PDB accession 1CMK) and substrate-bound (blue; PDB accession 3FJQ), with ATP (red) as spheres. In the right two panels, the absolute magnitude of directional flux J is mapped onto the apo structure, using the same thresholds as for ADK.

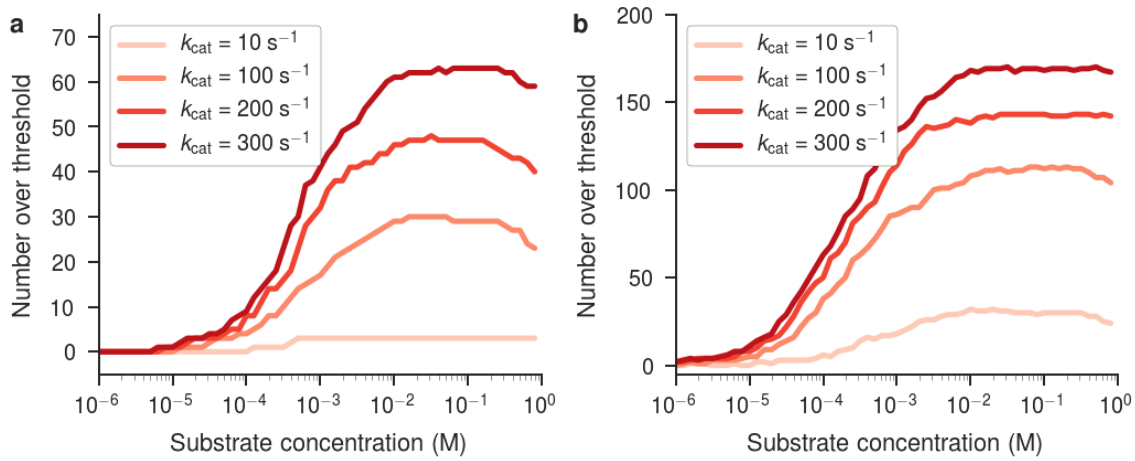

Fig. S3. Number of HIVP torsion angles with net flux magnitude, $|J|$, above a given threshold, as a function of substrate concentration, for various assumed values of k_{cat}. (a) The number of torsions with $|J| > 1$ cycle s^{-1} (b) The number of torsions with $|J| > 0.1$ cycle s^{-1}.

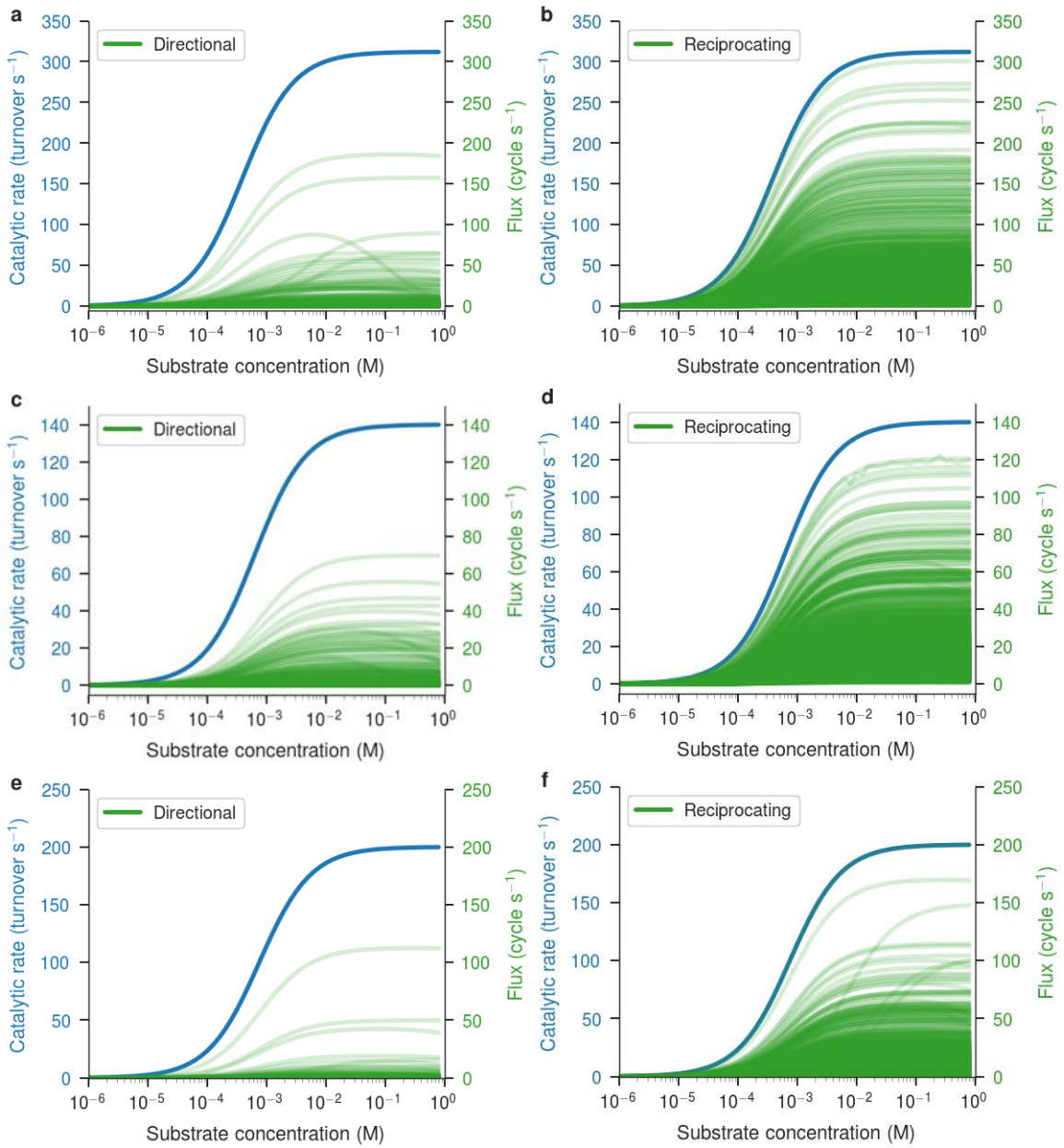

Fig. S4. The dependence of the catalytic rate (blue) and flux (green) on substrate concentration. (a-b) All angles in ADK, calculated with k_{cat} = 312 s^{-1}. (c-d) All angles in PKA, calculated with k_{cat} = 140 s^{-1}. (e-f) All angles in HIVP, calculated with k_{cat} = 200 s^{-1}. Reciprocating flux is shown only for angles with a maximum directional flux below 1 cycle s^{-1}.

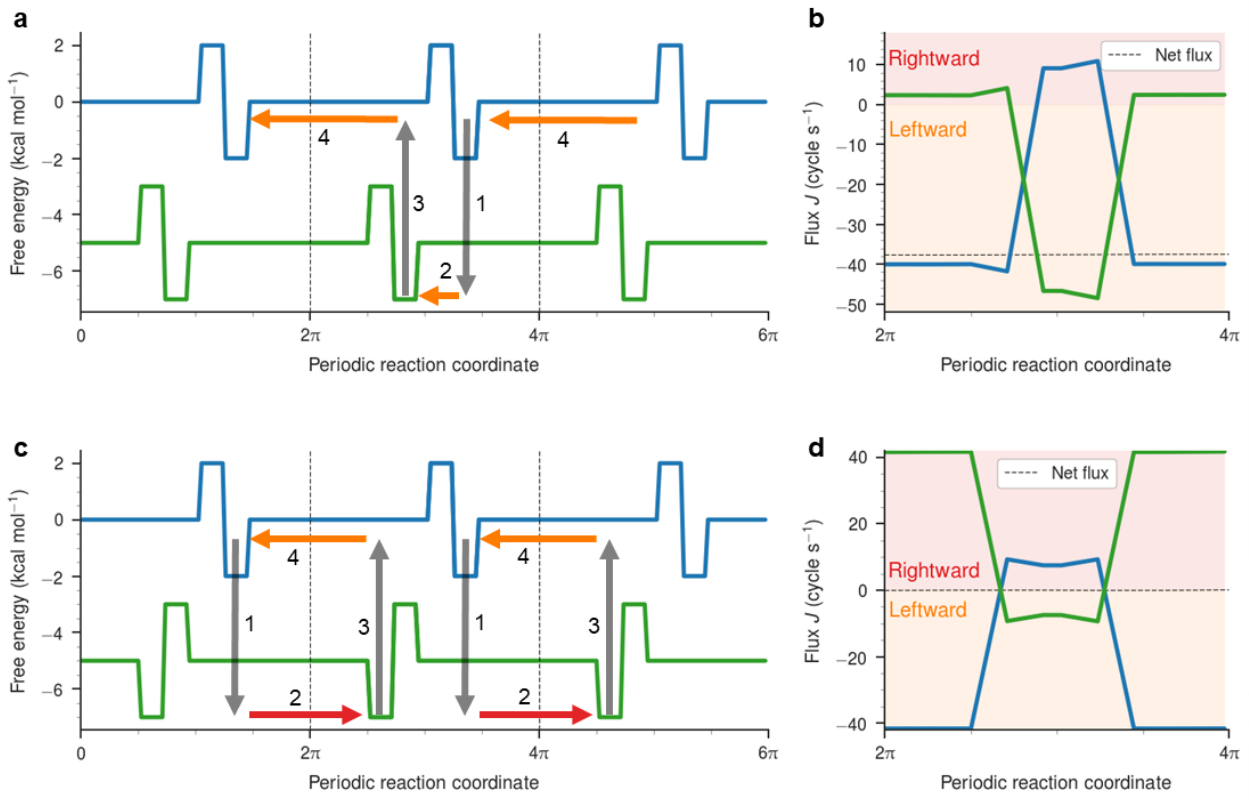

Fig. S5. Sample periodic energy surfaces, each containing one barrier and one minimum per cycle, illustrating predominant directional or reciprocating net flux, depending on the relative positioning of the barriers and minima. (a-b) Energy surfaces that show net "left" directional flux J, when the probability is able to bypass the barrier on one surface by transitioning to the other surface. (c-d) Energy surfaces that show no directional net flux, but high reciprocating flux J_R, arising from closed loops of probability flow.

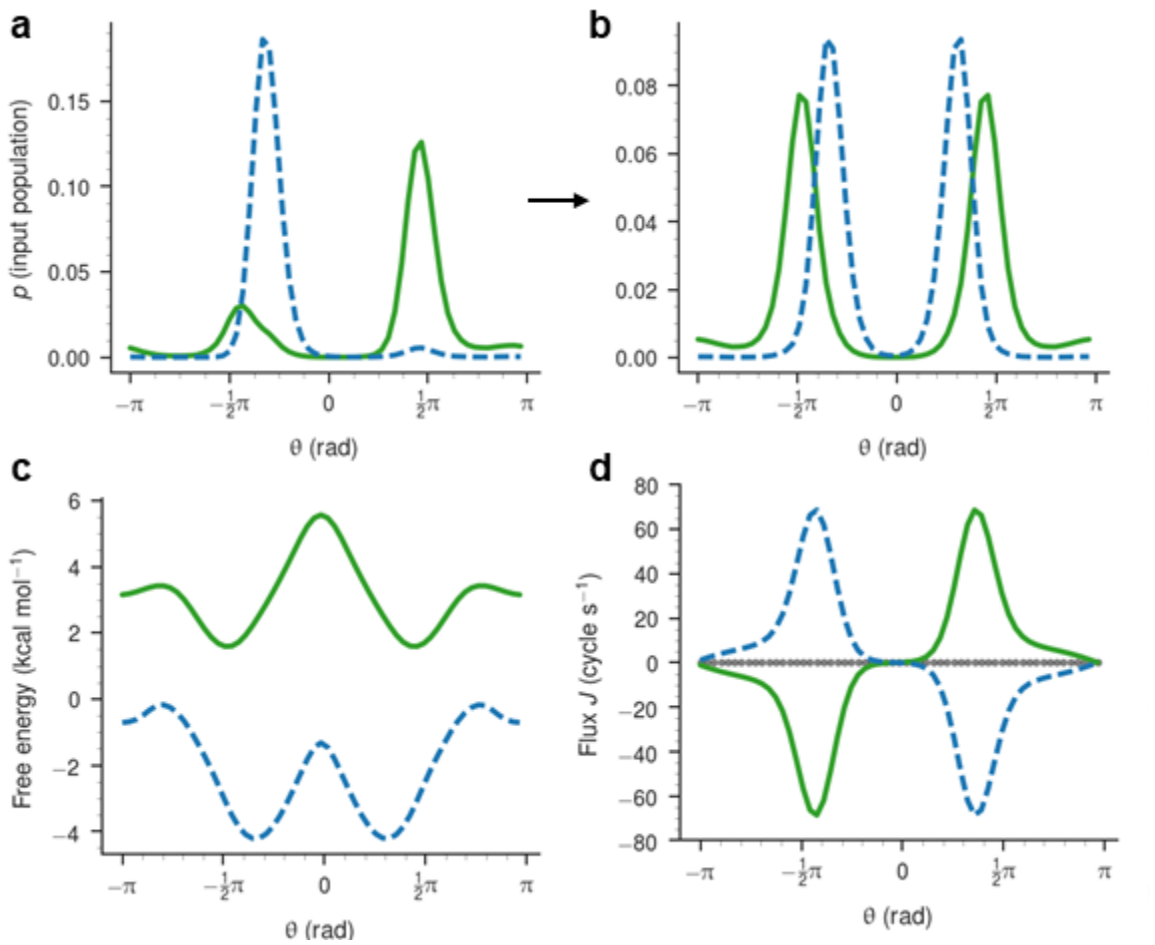

Fig. S6. The effect of symmetrizing the energy landscape of the χ_2 angle of ADK Thr175 on directional flux. (a) Unmodified probability distributions for the apo (green) and bound (blue) state of the torsion (also drawn in Fig. 3b). (b) The result of averaging each population histogram with its reflection about $\theta = 0$ rad. (c) Free energy surfaces corresponding to the population densities in panel b (cf. Fig. 3c). The probability flux drawn separately for each surface and as a sum (grey points), showing exactly zero directional flux due the symmetry of the two energy surfaces (cf. Fig. 3d).

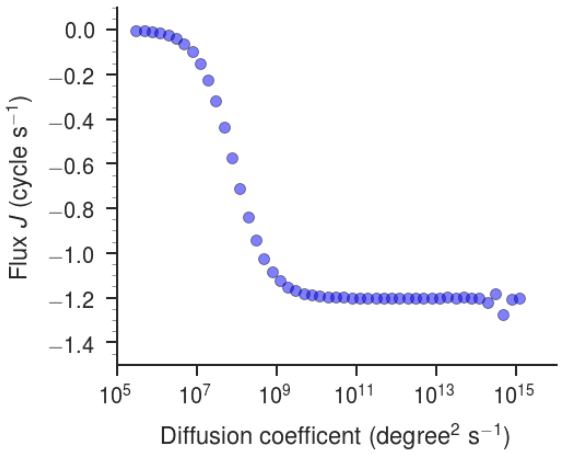

Fig. S7. Flux as a function of the diffusion coefficient D for the χ_2 angle of Thr175 in ADK.

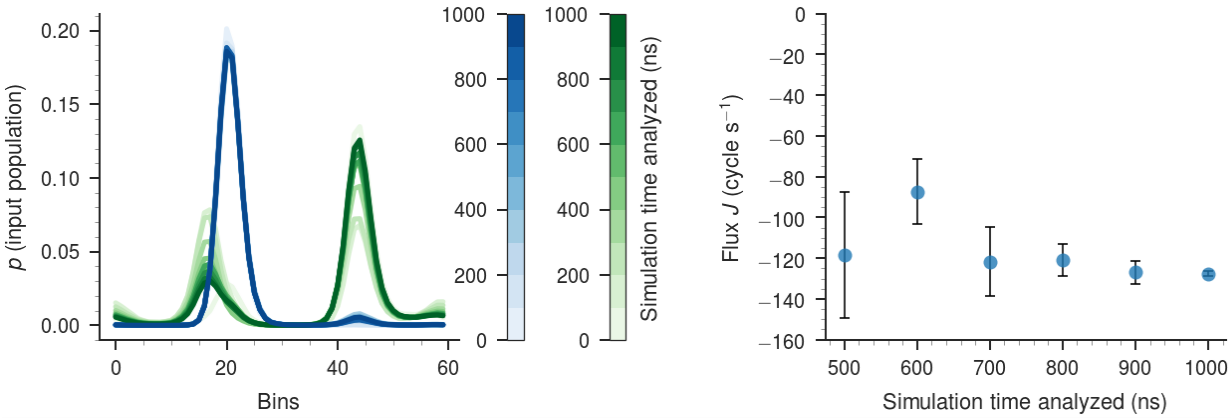

Fig. S8. The convergence of the population histograms for the χ_2 angle of Thr175 in ADK during equilibrium MD simulations for the apo (green) and bound (blue) states (left). The net flux calculated for this angle using the histograms on the left, after 500, 600, 700, 800, 900, and 1000 ns (right). The error bars represent the value of the net flux obtained after analyzing only the first or second half of each interval.

Table S1. Values of enzymatic parameters used in the present calculations.

	K_d (M)	$RT \ln K_d$ (kcal mol^{-1})	k_{on} (M^{-1} s^{-1})	k_{cat} (s^{-1})
PKA	4.0×10^{-5} [a]	-6.0	2.4×10^{6} [b]	140 [c]
ADK	6.8×10^{-5} [d]	-5.7	10^{6} [e]	312 [f]
HIVP	5.3×10^{-4} [g]	-4.5	10^{6} [h]	10 [i]

[a] K_d for ATP in Scheme 4 in (39).
[b] k_1 in Scheme 4 in (39).1xA9k
[c] The kinetics of PKA are complex and depend on, among other factors, the presence of divalent ion species and occupancy in the active site. The observed catalytic rate includes two or more conformational changes and lies between 50 s^{-1} and a fast, burst-phase of 500 s^{-1}. We used the rate-limiting step (ADP · P_i release) from Figure 11 of (13) in this manuscript.
[d] An average of K_d values for ATP found in (12) and (40). The calculated μ_{offset} is an average of the μ_{offset} for each K_d. The K_d values for AMP are roughly four times as large. Our model implicitly assumes a single substrate and single on rate.
[e] An order of magnitude estimate calculated using K_M from (9), k_{cat} values from (9) and (10), with the median expected ATP k_{off} from (12), and using the relationship $k_{\text{on}} = \frac{k_{\text{off}} + k_{\text{cat}}}{K_M} = (4.2 \text{ to } 5.7) \times 10^6 \text{ M}$, assuming Michaelis-Menten kinetics.
[f] An average of k_{cat} from (9) and (10).
[g] A literature value of K_d for the specific Gag fragment used in the simulations was not found in the literature. However, reference (41) reports $K_M = 5.3 \times 10^{-4}$ M for the p1/p6 substrate sequence PGNFLQS (the simulated bound peptide sequence was RPGNFLQSRP) and for sufficiently small catalytic rate, $K_{\text{d}} \sim K_{\text{M}}$. Several other references list values for k_{cat} / K_M.
[h] No value could be found in the literature, so the same order of magnitude as ADK is used.
[i] Catalytic rates as low as 0.3 s^{-1} are reported in (41) for the p1/p6 substrate sequence, but other Gag sequences have catalytic rates on the order of 10 s^{-1}, see for example (15-17).

Table S2. Torsion angle definitions, using atom types from Amber ff14SB.

Residue	Angle	Atom 1	Atom 2	Atom 3	Atom 4
ALA	phi	C	N	CA	C
ALA	psi	N	CA	C	N
ALA	chi1	HB1	CB	CA	N
ARG	phi	C	N	CA	C
ARG	psi	N	CA	C	N
ARG	chi1	CG	CB	CA	N
ARG	chi2	CD	CG	CB	CA
ARG	chi3	NE	CD	CG	CB
ARG	chi4	CZ	NE	CD	CG
ARG	chi5	NH1	CZ	NE	CD
ASN	phi	C	N	CA	C
ASN	psi	N	CA	C	N
ASN	chi1	CG	CB	CA	N
ASN	chi2	ND2	CG	CB	CA
ASP	phi	C	N	CA	C
ASP	psi	N	CA	C	N
ASP	chi1	CG	CB	CA	N
ASP	chi2	OD2	CG	CB	CA
CYS	phi	C	N	CA	C
CYS	psi	N	CA	C	N
CYS	chi1	SG	CB	CA	N
CYS	chi2	HG	SG	CB	CA
GLN	phi	C	N	CA	C
GLN	psi	N	CA	C	N
GLN	chi1	CG	CB	CA	N
GLN	chi2	CD	CG	CB	CA
GLN	chi3	NE2	CD	CG	CB
GLN	chi4	HE21	NE2	CD	CG
GLU	phi	C	N	CA	C
GLU	psi	N	CA	C	N
GLU	chi1	CG	CB	CA	N
GLU	chi2	CD	CG	CB	CA
GLU	chi3	OE1	CD	CG	CB
GLY	phi	C	N	CA	C
GLY	psi	N	CA	C	N
HIS	phi	C	N	CA	C
HIS	psi	N	CA	C	N
HIS	chi1	CG	CB	CA	N
HIS	chi2	CD2	CG	CB	CA
ILE	phi	C	N	CA	C

ILE	psi	N	CA	C	N
ILE	chi1	CG1	CB	CA	N
ILE	chi2	CD1	CG1	CB	CA
LEU	phi	C	N	CA	C
LEU	psi	N	CA	C	N
LEU	chi1	CG	CB	CA	N
LEU	chi2	CD1	CG	CB	CA
LYS	phi	C	N	CA	C
LYS	psi	N	CA	C	N
LYS	chi1	CG	CB	CA	N
LYS	chi2	CD	CG	CB	CA
LYS	chi3	CE	CD	CG	CB
LYS	chi4	NZ	CE	CD	CG
MET	phi	C	N	CA	C
MET	psi	N	CA	C	N
MET	chi1	CG	CB	CA	N
MET	chi2	SD	CG	CB	CA
MET	chi3	CE	SD	CG	CB
PHE	phi	C	N	CA	C
PHE	psi	N	CA	C	N
PHE	chi1	CG	CB	CA	N
PHE	chi2	CD1	CG	CB	CA
PRO	phi	C	N	CA	C
PRO	psi	N	CA	C	N
PRO	chi1	CG	CB	CA	N
PRO	chi2	CD	CG	CB	CA
PRO	chi3	N	CD	CG	CB
SER	phi	C	N	CA	C
SER	psi	N	CA	C	N
SER	chi1	OG	CB	CA	N
THR	phi	C	N	CA	C
THR	psi	N	CA	C	N
THR	chi1	CG2	CB	CA	N
THR	chi2	HG1	OG1	CB	CA
TRP	phi	C	N	CA	C
TRP	psi	N	CA	C	N
TRP	chi1	CG	CB	CA	N
TRP	chi2	CD1	CG	CB	CA
TYR	phi	C	N	CA	C
TYR	psi	N	CA	C	N
TYR	chi1	CG	CB	CA	N
TYR	chi2	CD1	CG	CB	CA
TYR	chi3	HH	OH	CZ	CE1

VAL	phi	C	N	CA	C
VAL	psi	N	CA	C	N
VAL	chi1	CG1	CB	CA	N

References

1. Astumian, R. D. 1997. Thermodynamics and kinetics of a Brownian motor. Science 276:917-922.
2. Astumian, R. D., and M. Bier. 1994. Fluctuation driven ratchets: Molecular motors. Phys Rev Lett 72:1766-1769.
3. Kay, E. R., D. A. Leigh, and F. Zerbetto. 2007. Synthetic molecular motors and mechanical machines. Angew Chem Int Ed Engl 46:72-191.
4. Wang, H., and G. Oster. 2002. Ratchets, power strokes, and molecular motors. Applied Physics A 75:315-323.
5. Astumian, R. D. 2016. Optical vs. chemical driving for molecular machines. Faraday Discuss.
6. Astumian, R. D. 2011. Stochastic conformational pumping: a mechanism for free-energy transduction by molecules. Annu Rev Biophys 40:289-313.
7. Astumian, R. D. 2014. Enhanced diffusion, chemotaxis, and pumping by active enzymes: progress toward an organizing principle of molecular machines. ACS Nano 8:11917-11924.
8. Riemann, P. 2002. Brownian motors: noisy transport far from equilibrium. Physics Reports.
9. Aden, J., A. Verma, A. Schug, and M. Wolf-Watz. 2012. Modulation of a Pre-existing Conformational Equilibrium Tunes Adenylate Kinase Activity. J. Am. Chem. Soc. 134:16562-16570.
10. Wolf-Watz, M., V. Thai, K. Henzler-Wildman, G. Hadjipavlou, E. Z. Eisenmesser, and D. Kern. 2004. Linkage between dynamics and catalysis in a thermophilic-mesophilic enzyme pair. Nat. Struct. Mol. Biol. 11:945-949.
11. Gerstein, M., G. Schulz, and C. Chothia. 1993. Domain closure in adenylate kinase. Joints on either side of two helices close like neighboring fingers. J. Mol. Biol. 229:494-501.
12. Hanson, J. A., K. Duderstadt, L. P. Watkins, S. Bhattacharyya, J. Brokaw, J. W. Chu, and H. Yang. 2007. Illuminating the mechanistic roles of enzyme conformational dynamics. Proc Natl Acad Sci U S A 104:18055-18060.
13. Adams, J. A. 2001. Kinetic and catalytic mechanisms of protein kinases. Chem Rev 101:2271-2290.
14. McClendon, C. L., A. P. Kornev, M. K. Gilson, and S. S. Taylor. 2014. Dynamic architecture of a protein kinase. Proc Natl Acad Sci U S A 111:E4623-4631.
15. Wondrak, E. M., J. M. Louis, and S. Oroszlan. 1991. The Effect of Salt on the Michaelis Menten Constant of the Hiv-1 Protease Correlates with the Hofmeister Series. FEBS Lett. 280:344-346.
16. Windsor, I. W., and R. T. Raines. 2015. Fluorogenic Assay for Inhibitors of HIV-1 Protease with Sub-picomolar Affinity. Sci Rep 5:11286.
17. Pokorna, J., J. Heyda, and J. Konvalinka. 2013. Ion specific effects of alkali cations on the catalytic activity of HIV-1 protease. Faraday Discuss 160:359-370; discussion 389-403.
18. Scott, W. R. P., and C. A. Schiffer. 2000. Curling of Flap Tips in HIV-1 Protease as a Mechanism for Substrate Entry and Tolerance of Drug Resistance. Structure 8:1259-1265.

19. Kurt, N., W. R. P. Scott, C. A. Schiffer, and T. Haliloglu. 2003. Cooperative fluctuations of unliganded and substrate-bound HIV-1 protease: A structure-based analysis on a variety of conformations from crystallography and molecular dynamics simulations. Proteins 51:409-422.
20. Coskun, A., M. Banaszak, R. D. Astumian, J. F. Stoddart, and B. A. Grzybowski. 2012. Great expectations: can artificial molecular machines deliver on their promise? Chem Soc Rev 41:19-30.
21. Howard, J. 2009. Motor Proteins as Nanomachines: The Roles of Thermal Fluctuations in Generating Force and Motion. Seminaire Poincare.
22. Bustamante, C., D. Keller, and G. Oster. 2001. The physics of molecular motors. Acc Chem Res 34:412-420.
23. Keller, D., and C. Bustamante. 2000. The mechanochemistry of molecular motors. Biophys. J. 78:541-556.
24. Riedel, C., R. Gabizon, C. A. Wilson, K. Hamadani, K. Tsekouras, S. Marqusee, S. Presse, and C. Bustamante. 2015. The heat released during catalytic turnover enhances the diffusion of an enzyme. Nature 517:227-230.
25. Muddana, H. S., S. Sengupta, T. E. Mallouk, A. Sen, and P. J. Butler. 2010. Substrate catalysis enhances single-enzyme diffusion. J. Am. Chem. Soc. 132:2110-2111.
26. van der Walt, S., S. C. Colbert, and G. Varoquaux. 2011. The NumPy Array: A Structure for Efficient Numerical Computation. Comput Sci Eng 13:22-30.
27. Olivier, B. G., J. M. Rohwer, and J. H. Hofmeyr. 2002. Modelling cellular processes with Python and Scipy. Mol. Biol. Rep. 29:249-254.
28. Muller, C. W., G. J. Schlauderer, J. Reinstein, and G. E. Schulz. 1996. Adenylate kinase motions during catalysis: an energetic counterweight balancing substrate binding. Structure 4:147-156.
29. Unni, S., Y. Huang, R. M. Hanson, M. Tobias, S. Krishnan, W. W. Li, J. E. Nielsen, and N. A. Baker. 2011. Web servers and services for electrostatics calculations with APBS and PDB2PQR. J Comput Chem 32:1488-1491.
30. Schrank, T. P., D. W. Bolen, and V. J. Hilser. 2009. Rational modulation of conformational fluctuations in adenylate kinase reveals a local unfolding mechanism for allostery and functional adaptation in proteins. Proc Natl Acad Sci U S A 106:16984-16989.
31. Jakalian, A., B. L. Bush, D. B. Jack, and C. I. Bayly. 2000. Fast, efficient generation of high-quality atomic charges. AM1-BCC model: I. Method. Journal of Computational Chemistry 21:132-146.
32. Wang, J., and H. Tingjun. 2011. Application of Molecular Dynamics Simulations in Molecular Property Prediction I: Density and Heat of Vaporization. J Chem Theory Comput 7:2151-2165.
33. Wang, J., R. M. Wolf, J. W. Caldwell, P. A. Kollman, and D. A. Case. 2004. Development and testing of a general amber force field. J Comput Chem 25:1157-1174.
34. Hopkins, C. W., S. Le Grand, R. C. Walker, and A. E. Roitberg. 2015. Long-Time-Step Molecular Dynamics through Hydrogen Mass Repartitioning. J Chem Theory Comput 11:1864-1874.

35. D.A. Case, R. M. B., W. Botello-Smith, D.S. Cerutti, T.E. Cheatham, III, T.A. Darden, R.E. Duke, T.J. Giese, H. Gohlke, A.W. Goetz, N. Homeyer, S. Izadi, P. Janowski, J. Kaus, A. Kovalenko, T.S. Lee, S. LeGrand, P. Li, C. Lin, T. Luchko, R. Luo, B. Madej, D. Mermelstein, K.M. Merz, G. Monard, H. Nguyen, H.T. Nguyen, I. Omelyan, A. Onufriev, D.R. Roe, A. Roitberg, C. Sagui, C.L. Simmerling, J. Swails, R.C. Walker, J. Wang, R.M. Wolf, X. Wu, L. Xiao, D.M. York and P.A. Kollman. 2016. AMBER 2016. In University of California, San Francisco.
36. Roe, D. R., and T. E. Cheatham, 3rd. 2013. PTRAJ and CPPTRAJ: Software for Processing and Analysis of Molecular Dynamics Trajectory Data. J Chem Theory Comput 9:3084-3095.
37. Spinelli, S., Q. Z. Liu, P. M. Alzari, P. H. Hirel, and R. J. Poljak. 1991. The three-dimensional structure of the aspartyl protease from the HIV-1 isolate BRU. Biochimie 73:1391-1396.
38. Prabu-Jeyabalan, M., E. Nalivaika, and C. A. Schiffer. 2002. Substrate shape determines specificity of recognition for HIV-1 protease: analysis of crystal structures of six substrate complexes. Structure 10:369-381.
39. Shaffer, J., and J. A. Adams. 1999. An ATP-linked structural change in protein kinase A precedes phosphoryl transfer under physiological magnesium concentrations. Biochemistry 38:5572-5581.
40. Aden, J., and M. Wolf-Watz. 2007. NMR identification of transient complexes critical to adenylate kinase catalysis. J. Am. Chem. Soc. 129:14003-14012.
41. Abram, M. E. 2005. Proteolytic cleavage events in the maturation of HIV-1 reverse transcriptase. University of Pittsburgh.